PHOTONICS Research

High-resolution dual-polarization single-pixel imaging through dynamic and complex scattering media using random-frequency-encoded time sequences

ZIAN WANG,[1,2] TIANSHUN ZHANG,[1] YIN XIAO,[1] ZHIGANG LIU,[2,3] AND WEN CHEN[1,*]

[1] *Department of Electrical and Electronic Engineering, The Hong Kong Polytechnic University, Hong Kong SAR, China*
[2] *Key Laboratory of Education Ministry for Modern Design and Rotor-Bearing System, Xi'an Jiaotong University, Xi'an 710049, China*
[3] *e-mail: mezgliu@mail.xjtu.edu.cn*
**Corresponding author: owen.chen@polyu.edu.hk*

Received 3 June 2025; revised 21 July 2025; accepted 23 July 2025; posted 23 July 2025 (Doc. ID 569507); published 26 September 2025

Single-pixel imaging (SPI) through complex media remains challenging. In this paper, we report high-resolution common-path SPI with dual polarization using random-frequency-encoded time sequences in complex environments where the illumination and detection paths are severely distorted. By leveraging a common-path optical configuration with orthogonal polarization states, a series of dynamic scaling factors can be corrected. The designed random-frequency encoding scheme disperses scattering-induced noise into artifacts to be simply removed. It is demonstrated in optical experiments that the proposed method is feasible and effective to reconstruct high-resolution object images in complex environments. The proposed method does not require complex optical components and prior knowledge about scattering media, providing a robust solution for high-resolution optical imaging in complex scenarios where the illumination and detection paths are severely distorted at the same time.

https://doi.org/10.1364/PRJ.569507

1. INTRODUCTION

Enhancing the imaging quality in scattering environments remains a challenge in optics [1–8]. The inherent inhomogeneity of scattering media induces multiple refractions, distorting the wavefront [9]. This phenomenon fundamentally limits optical imaging, as real-world scenes could exhibit complex and dynamic scattering behaviors. To address wavefront restoration, numerous approaches have been reported, e.g., memory effect [10–12], ballistic light imaging [13–16], matrix transfer inversion [17–19], and optical phase conjugation [20–23]. Among these, single-pixel imaging (SPI) has emerged to be promising for solving scattering problems [24–27], primarily due to its reliance on light intensity fluctuations for object reconstruction. Previous studies have demonstrated that SPI achieves high-quality reconstruction, when static scattering media are placed in the optical channel. Although SPI performs well in scattering media, it still faces a challenge when applied in complex environments, i.e., simultaneous distortions of illumination and detection paths.

When dynamic scattering media exist between the light source and an object in the illumination path, the scattering degrades illumination patterns, causing them to deviate from the pre-designed ones [28]. Furthermore, dynamic scattering media would induce a series of dynamic scaling factors that disrupt beam correlation [29] and lead to a failure of SPI. Therefore, SPI in dynamic scattering media remains a challenge, requiring robust reconstructions while preserving computational efficiency. While deep learning [30–32] and iterative algorithms [33,34] have yielded promising results, they could depend on prior knowledge about scattering media and suffer from high computational cost. Correlation imaging [28,35] can enable object reconstruction in static scattering environments. However, its feasibility in dynamic scattering environments remains unexplored, and a further improvement of imaging quality is required. The strategies via a design of illumination patterns (e.g., Hadamard [36], Fourier coefficients [37]) have also been developed and applied. However, in dynamic scattering environments where illumination and detection paths are distorted, previous single-pixel detection techniques relying on the light intensity collection would fail. Other approaches, such as rotating ground glass with CCD-based pattern recording [38], can address pattern degradation problems but still face the limitations in real-world scenarios. It is well recognized that when the illumination and detection paths are severely distorted, high-resolution SPI remains not to be explored.

In this paper, we report high-resolution common-path SPI with dual polarizations that integrates an optical design with random-frequency-encoded time sequences to overcome the challenge in dynamic and complex scattering environments. The method employs a common-path optical configuration with dual polarizations (s- and p-polarized light beams), leading to the path consistency for correcting a series of dynamic scaling factors induced by complex media existing in the illumination and detection paths. To solve the pattern degradation problem caused by dynamic scattering media in the illumination path, a series of random-frequency-encoded time sequences are designed via assigning each pixel along the time axis a random frequency. Via the design of a common-path dual-polarization setup, the effect of the scattering media can be suppressed. During object reconstruction, fast Fourier transform (FFT) can be performed on the corrected single-pixel light intensities. Each pixel value in a reconstructed object image is obtained with a generated amplitude spectrum identified via the pixel position pre-defined with a specific encoding frequency. Scattering-induced noise can be dispersed into artifacts that are removed simply using a mean filter. The proposed method does not require prior knowledge about scattering media, and complex optical components are also not needed. Experimental results demonstrate its superiority over existing methods in achieving high-resolution optical imaging under complex conditions where illumination and detection paths are severely distorted at the same time.

2. PRINCIPLE

Figure 1 shows the principle of the developed SPI system based on a random-frequency encoding scheme with dual polarizations and a common path. A series of time sequences with values in a range of 0–1 is generated, and each time sequence is assigned a random frequency as shown in Fig. 1(a). A generated time sequence is used for a specific pixel along the time axis, and at an instant t we have

$$\beta_{xy} = 0.5 \sin\left(2\pi f_{xy} \frac{t}{f_s}\right) + 0.5, \tag{1}$$

where xy denotes a 2D coordinate of the pixels, f_{xy} denotes a frequency randomly assigned for a time sequence (i.e., a pixel along the time axis), and f_s denotes a sampling ratio. To avoid the aliasing, a relationship of $f_s \geqslant 2f_{\max}$ is adopted to satisfy the Nyquist sampling theorem, where $f_{\max}$ denotes the maximum value of f_{xy}. Here, parameter f_{xy} is randomly set in a range of 1.0–4096.0 Hz with an interval of 1.0 Hz. The frequency interval could be enlarged for easily decoding the frequencies during the reconstruction. As shown in Fig. 1(b), after all time sequences are generated, a series of 2D random patterns can be correspondingly obtained and each pixel along the time axis has a unique frequency identity. The light beam is split by PBS1 into s- and p-polarized light beams with mutually perpendicular polarization states. The s-polarized light beam is sequentially modulated by a series of 2D random patterns embedded into a spatial light modulator (SLM), and the p-polarized light beam is reflected by a mirror. Then, the light beams pass through complex scattering media in a common path where the illumination and detection are simultaneously distorted.

After wave propagation through dynamic scattering media existing in the illumination and detection paths, PBS2 is used to separate the s- and p-polarized light beams and the intensity of s-polarized light recorded by a single-pixel bucket detector can be described by

$$I_s = k_t \sum_x \sum_y [(\alpha I_1 \beta_{xy} + I_{c-xy}) O_{xy}], \tag{2}$$

where α denotes the light transmittance in the illumination path through scattering media, k_t denotes dynamic scaling factors induced by complex media at an instant t, O denotes the transmission matrix of an object, and I_1 and I_{c-xy} denote the s-polarized light intensity incident to SLM and scattered light intensity onto an object, respectively. The complex media in the illumination path cause the degradation of illumination

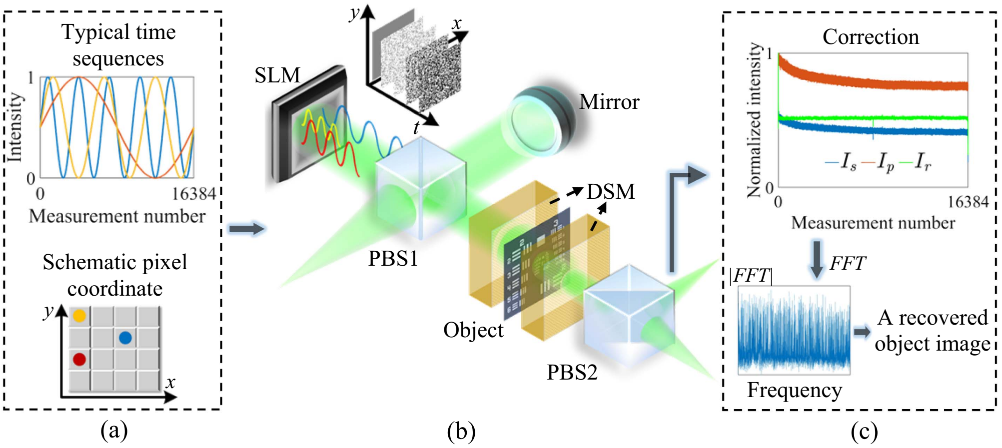

Fig. 1. A flow chart of the developed dual-polarization common-path SPI with random-frequency-encoded time sequences in dynamic and complex scattering media where illumination and detection paths are severely distorted: (a) typical time sequences generated for each pixel along the time axis having random frequencies, (b) a designed common-path SPI scheme with dual polarizations (PBS, polarization beam splitter; DSM, dynamic scattering media), and (c) the object reconstruction process.

patterns. Then, distorted optical waves propagate through the object and another complex scattering medium. The illumination and detection paths are severely distorted at the same time, leading to a failure of conventional SPI methods. The p-polarized light beam is reflected by a mirror, and is collected by another single-pixel bucket detector described by

$$I_p = k_t \sum_x \sum_y [(\alpha I_2 + I_{c-xy}) O_{xy}], \tag{3}$$

where I_2 denotes intensity of the p-polarized light beam reflected by the mirror. At an instant t, the collected single-pixel light intensities I_s and I_p are obtained after the same degradations with the same scaling factors, since a common path is applied. Therefore, parameters k_t, α, and I_{c-xy} can be assumed as the same for light intensities I_s and I_p at an instant t. The series of dynamic scaling factors k_t induced by scattering media can be removed by

$$I_r = \frac{I_s}{I_p} = \frac{\sum_x \sum_y [(\alpha I_1 \beta_{xy} + I_{c-xy}) O_{xy}]}{\sum_x \sum_y [(\alpha I_2 + I_{c-xy}) O_{xy}]}, \tag{4}$$

where I_r denotes a corrected light intensity.

After an FFT operation is performed on Eq. (4), we can have (see details in Appendix A)

$$\mathrm{FFT}(I_r) \propto \sum \sum \delta(\xi - f_{xy}/f_s) O + \sum \sum W O, \tag{5}$$

where W denotes noise with a Gaussian distribution. It is indicated in Eq. (5) that I_{c-xy} serves as Gaussian-distributed noise. Then, each amplitude spectrum $|\mathrm{FFT}(I_r)|$ is directly assigned to a corresponding pixel to obtain a reconstructed 2D object image according to the pixel position pre-defined with the specific encoding frequency. Finally, noise in the reconstructed 2D object image can be simply removed via a mean filter. The object reconstruction process is shown in Fig. 1(c). In practice, a spectrum optimization algorithm may be further used to enhance frequency identification accuracy. Here, the FFT operation is directly employed to illustrate the effectiveness of the proposed method.

3. EXPERIMENTAL RESULTS AND DISCUSSION

A. Proof-of-Principle Experiment

To validate the proposed method, a complex scene is designed and employed in optical experiments. As shown in Fig. 2, an amplitude-only SLM with pixel size of 4.5 μm is sequentially loaded with 16,384 2D random patterns, i.e., $f_s = 4f_{\max}$ as 16,384 in Eq. (1). A diode-pumped green laser (CrystaLaser, CL532-025-S) is expanded by an objective lens (40×) to illuminate SLM, and then the loaded patterns can be projected onto an object placed between two established dynamic scattering environments. Here, original patterns with 64 × 64 pixels are linearly interpolated to be 512 × 512 pixels to satisfy experimental requirements. The dynamic scattering medium placed in the illumination path is established by using a ground glass diffuser (Thorlabs, DG10-1500) being kept rotating. The dynamic scattering medium placed in the detection path is established by using 3.0-mL skimmed milk (diluted with 200.0-ml clean water) to be continuously dripped into a water tank [dimensions of 10.0 cm (length) × 15.0 cm (width) × 30.0 cm (height)] initially filled with 3000-mL clean water in each experiment, and a stirrer with a speed of 400 r/min is used to generate a dynamic environment inside the water tank. Here, the Beer-Lambert law [39] is used to quantitatively analyze the effect of the water tank placed in the detection path, and the Beer's coefficient gradually increases to $8.9 \times 10^{-3}\ \mathrm{mm}^{-1}$ in experiments. At the detection plane, light intensities in the s- and p-polarized light beam paths are simultaneously recorded by using two single-pixel detectors (Thorlabs, PDA100A2).

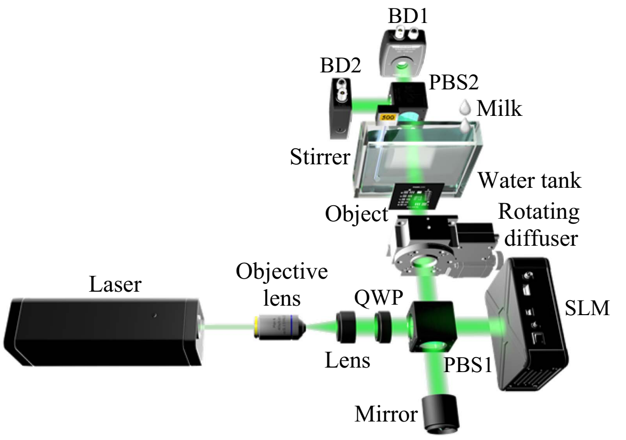

Fig. 2. Schematic of an experimental setup to validate the proposed method. Two lenses with the same focal length of 150.0 mm are used as a 4f system between the SLM and object, and are omitted for sake of brevity. QWP: quarter wave plate; BD: single-pixel bucket detector.

An object, i.e., Group 2 Elements 2 and 3 of USAF 1951 resolution target, is first tested. Figure 3(a) shows a reconstructed object image using the proposed method for a comparison, when no scattering media are used in Fig. 2. Figure 3(b) shows a reconstructed object image obtained by using the proposed method in dynamic and complex scattering media as shown in Fig. 2, and the reconstructed object image after the further use of a mean filter is shown in Fig. 3(c). Contrast-to-noise ratio (CNR) [40] is calculated to quantify the imaging quality with a signal area (red box) and a background area (green box) indicated in Fig. 3(a). To ensure the consistency and rationality, the same signal and background areas are applied to evaluate experimental results. The CNR value in Fig. 3(a) is 21.37, and CNR values in Figs. 3(b) and 3(c) are 10.34 and 17.28, respectively. It is demonstrated that the proposed method can be used to recover high-quality object images, and is robust against dynamic complex scattering media where the illumination and detection paths are severely

(a) (b) (c)

Fig. 3. Experimental results: (a) a reconstructed object image obtained by using the proposed method without any scattering media placed in the optical setup in Fig. 2, (b) a reconstructed object image obtained by using the proposed method through dynamic scattering media composed of the rotating diffuser and the water tank, and (c) a reconstructed object image after the further use of a mean filter to (b).

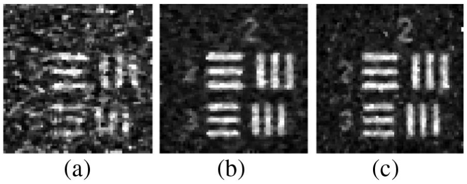

Fig. 4. Experimental results: (a)–(c) the reconstructed object images obtained by using the proposed method respectively at a sampling ratio of $f_{\max}$, $2f_{\max}$, and $3f_{\max}$.

distorted at the same time. It is also verified in experiments that noise appears in the form of pixel-level artifacts as shown in Fig. 3(b), and the reconstruction quality can be enhanced via a simple use of the mean filter.

B. Different Sampling Ratios

To evaluate performance of the proposed method at different sampling ratios, experimental results are obtained and shown in Figs. 3(c) and 4(a)–4(c). The CNR values in Figs. 3(c) and 4(a)–4(c) are 17.28, 3.05, 9.09, and 11.38, when the sampling ratio f_s in Eq. (1) is set as $4f_{\max}$, $f_{\max}$, $2f_{\max}$, and $3f_{\max}$, respectively. It can be found in experiments that as the sampling rate decreases, quality of the reconstructed object images deteriorates using the proposed method. This is attributed to a reduction in frequency resolution used in the designed random-frequency encoding scheme. As given in Eq. (1), f_s is determined by the maximum value of f_{xy}. When f_s falls below $2f_{\max}$, the Nyquist sampling theorem is violated. This violation leads to frequency aliasing, resulting in a loss of high-frequency information, which ultimately causes a failure of object reconstruction. Therefore, it is essential to consider parameter f_s to make sure that the sampling theorem is satisfied.

C. Different Encoding Schemes

It is further illustrated why the random-frequency encoding scheme is adopted in the proposed method rather than the usage of a sequential-frequency encoding scheme in the proposed method, as shown in Fig. 5. In the sequential-frequency encoding scheme, time sequences for each pixel along the time axis are assigned the frequencies from 1.0 to 4096.0 Hz with an interval of 1.0 Hz in sequence. In experiments, the parameters are the same as those used in Figs. 2 and 3. The CNR values of the reconstructed object images in Figs. 5(b) and 5(d) are 17.28 and 14.40, when the random-frequency encoding and sequential-frequency encoding schemes are adopted in the proposed method, respectively. It is experimentally demonstrated that when the random-frequency encoding scheme is applied in the proposed SPI system, a higher-quality object image can be recovered. In addition, it can be observed that there is much noise at the bottom in Fig. 5(d). This is attributed to the diffraction effect induced by the usage of a sequential-frequency encoding scheme where the frequencies assigned for each pixel along the time axis are in sequence. As shown in Fig. 5(c), the sequential-frequency encoding scheme generates a series of patterns featuring varying numbers of fringes also with continuously varying directions. This implies that the sequential-frequency-encoded time sequences lead to the generation of diffraction orders with dynamically changing direction and spacing.

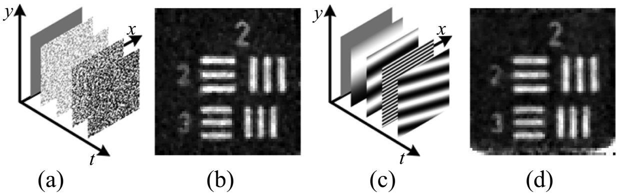

Fig. 5. Experimental results obtained by using random-frequency encoding and sequential-frequency encoding schemes in the proposed method: (a) a schematic of 2D patterns generated by using the random-frequency encoding scheme in the proposed method and (b) a reconstructed object image, and (c) a schematic of 2D patterns generated by using the sequential-frequency encoding scheme in the proposed method and (d) a reconstructed object image.

When the 2D patterns generated by using the sequential-frequency encoding scheme are used for the modulation in Fig. 2, the designed common path with dual polarizations could be disrupted. The sizes of illumination patterns in the s- and p-polarized light beam paths would not be the same, and the same dynamic scaling factors cannot be created at each instant. In addition, the devices used cannot cover all diffraction orders, causing a periodic modulation. In complex media where the illumination and detection paths are severely distorted, effective light intensities collected by single-pixel detectors undergo significant attenuations. Therefore, noise generated by the undetected higher-order diffraction components leads to a creation of relatively higher amplitudes in the Fourier domain. The low-frequency noise is induced, leading to those at the bottom of the reconstructed object image in Fig. 5(d). The random-frequency encoding scheme is designed and employed in the proposed method to minimize the diffraction effect due to the absence of fringe patterns, and the illumination patterns in the s- and p-polarized light beam paths can have the same size to enable an implementation of the designed common path with dual polarizations.

D. Performance

The existing SPI methods are further employed for comparisons, as shown in Fig. 6. The reconstructed object images obtained by using differential ghost imaging (DGI, a sampling ratio of 100%) [41,42] and Fourier SPI (FSI, a sampling ratio of 100%) [24] are shown in Figs. 6(a) and 6(b) with CNR values

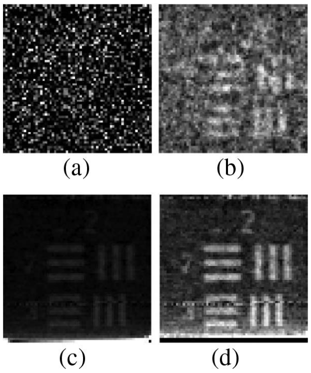

Fig. 6. The reconstructed object images obtained in experiments using (a) the DGI, (b) the FSI, (c) the STEP, and (d) a further removal of 128 pixels at the bottom of (c).

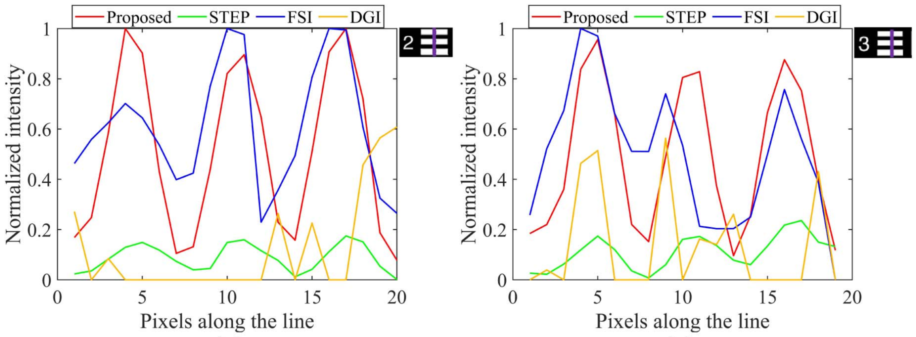

(a) (b)

Fig. 7. The profiles along the line (indicated in insets) of the reconstructed object images with a target of (a) Group 2 Element 2 and (b) Group 2 Element 3.

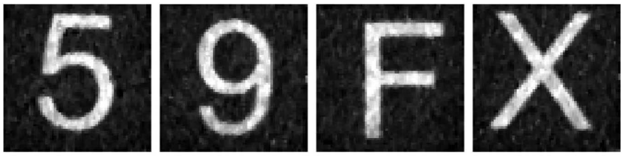

(a) (b) (c) (d)

Fig. 8. Experimental results: (a)–(d) the reconstructed object images obtained by using the proposed method.

of 0.48 and 2.52, respectively. It is experimentally demonstrated that DGI is totally incapable of recovering any effective object information, and the reconstruction result obtained by using FSI also fails to clearly render object information. This is attributed to the effects from simultaneous distortions of the illumination and detection paths. As shown in Fig. 6(c), when spatial-temporal encoded patterns (STEPs) [37] are used, the method is highly susceptible to the disturbances of dynamic scattering environments with very low contrast in the reconstructed object image. To visually render the details, 128 pixels at the bottom of Fig. 6(c) are further removed, and a reconstructed object image is obtained as shown in Fig. 6(d), which is contaminated by background noise. The CNR value in Fig. 6(d) is 10.23. Here, the proposed method can always be applied to reconstruct high-quality object images, such as with the CNR value of 17.28 in Fig. 3(c). It is experimentally demonstrated that the proposed method is feasible and effective in complex scenarios. Figures 7(a) and 7(b) show the profiles along a line (indicated in insets) of the reconstructed object images. Three peaks in Group 2 Element 2 or 3 can be clearly observed using the proposed method. High resolution, i.e., a line width of 99.21 μm, is achieved by using the proposed method.

Other targets are further tested using the proposed method with the optical setup in Fig. 2, and experimental results are shown in Figs. 8(a)–8(d). It is demonstrated again that the proposed method is feasible and effective in complex environments where illumination and detection paths are severely distorted at the same time.

4. CONCLUSION

We have reported high-resolution common-path SPI using dual polarizations and the random-frequency encoding scheme in complex scenarios. The proposed method leverages a dual-polarization common-path configuration to enable an accurate correction of dynamic scaling factors, and the random-frequency encoding scheme is designed and applied to encode information and distribute noise into pixel-level artifacts. Experimental validation shows high performance of the proposed method in complex scenes, and high resolution, i.e., 198.42 μm, is achieved with a high CNR of 17.28. The proposed method does not require complex optical components or prior knowledge about complex scattering media, and can pave the way for high-resolution optical imaging in complex scenarios where illumination and detection paths are severely distorted at the same time.

APPENDIX A

After performing an FFT operation on Eq. (4), we have

$$\begin{aligned}\mathrm{FFT}(I_r) &= \mathrm{FFT}\left\{\sum_x\sum_y[(\alpha I_1\beta_{xy}+I_{c\text{-}xy})O_{xy}]\right\}\\ &\quad *\mathrm{FFT}\left\{\frac{1}{\sum_x\sum_y[(\alpha I_2+I_{c\text{-}xy})O_{xy}]}\right\}\\ &= \mathrm{FFT}(A)*\mathrm{FFT}(B),\end{aligned}\tag{A1}$$

where $*$ denotes a convolution operation.

FFT(A) can be further described by

$$\mathrm{FFT}(A)=\mathrm{FFT}\left\{\sum_x\sum_y\left\{\left\{\alpha I_1\left[0.5\sin\left(2\pi f_{xy}\frac{t}{f_s}\right)+0.5\right]+I_{c\text{-}xy}\right\}O_{xy}\right\}\right\}\propto\sum\sum\delta(\xi-f_{xy}/f_s)O+\sum\sum WO,\tag{A2}$$

where W denotes noise with a Gaussian distribution. In Eq. (A2), since Fourier transform of a sine function is a centrally symmetric impulse function, only the half Fourier spectrum is further analyzed. It should be noted [43] that when Gaussian noise is Fourier transformed, Gaussian-distributed noise is still generated.

FFT(B) can be further described by

$$\begin{aligned}\mathrm{FFT}(B) &= \mathrm{FFT}\left\{\frac{1}{\sum_x\sum_y[(\alpha I_2 + I_{c-xy})O_{xy}]}\right\}\\ &= \mathrm{FFT}\left[\frac{1}{\sum_x\sum_y(\alpha I_2 O_{xy}) + \sum_x\sum_y(I_{c-xy}O_{xy})}\right]\\ &= \mathrm{FFT}\left(\frac{1}{C+D}\right).\end{aligned} \tag{A3}$$

Since C is a constant, the Taylor expansion and approximation can yield

$$\begin{aligned}\mathrm{FFT}(B) &= \mathrm{FFT}\left(\frac{1}{C}\right) - \mathrm{FFT}\left(\frac{D}{C^2}\right) + \mathrm{FFT}\left(\frac{D^2}{C^3}\right) - \cdots\cdots\\ &\approx \mathrm{FFT}\left(\frac{1}{C}\right) - \mathrm{FFT}\left(\frac{D}{C^2}\right)\\ &= -\frac{1}{C^2}\sum\sum WO.\end{aligned} \tag{A4}$$

It can be found that the resultant in Eq. (A4) conforms to a Gaussian distribution. It is explained that the resultant in Eq. (A4) can be approximately described by using impulse functions with the same amplitude spectrum, when the number of time sequences (or the number of frequencies f_{xy}) is large enough. Therefore, the convolution operation in Eq. (A1) can be treated as a constant multiplied by FFT(A), leading to the expression in Eq. (5).

Funding. National Natural Science Foundation of China (62405256); Hong Kong Research Grants Council General Research Fund (15224921, 15223522, 15237924); Hong Kong Research Grants Council Collaborative Research Fund (C5047-24G); Basic and Applied Basic Research Foundation of Guangdong Province (2023A1515010831, 2025A1515011411); The Hong Kong Polytechnic University (1-CDJA, 1-WZ4M).

Disclosures. The authors declare no conflicts of interest.

Data Availability. Data underlying the results presented in this paper are not publicly available at this time but may be obtained from the authors upon reasonable request.

REFERENCES

1. J. Yang, Q. He, L. Liu, *et al.*, "Anti-scattering light focusing by fast wavefront shaping based on multi-pixel encoded digital-micromirror device," Light Sci. Appl. **10**, 149 (2021).
2. L. Zhu, F. Soldevila, C. Moretti, *et al.*, "Large field-of-view non-invasive imaging through scattering layers using fluctuating random illumination," Nat. Commun. **13**, 1447 (2022).
3. Y. Shui, T. Wang, J. Zhou, *et al.*, "Scattered light imaging beyond the memory effect using the dynamic properties of thick turbid media," Adv. Photonics Nexus **2**, 026010 (2023).
4. Y. Jauregui-Sánchez, H. Penketh, and J. Bertolotti, "Tracking moving objects through scattering media via speckle correlations," Nat. Commun. **13**, 5779 (2022).
5. X. Wei, Y. Shen, J. C. Jing, *et al.*, "Real-time frequency-encoded spatiotemporal focusing through scattering media using a programmable 2D ultrafine optical frequency comb," Sci. Adv. **6**, eaay1192 (2020).
6. D. Wang, S. K. Sahoo, X. Zhu, *et al.*, "Non-invasive super-resolution imaging through dynamic scattering media," Nat. Commun. **12**, 3150 (2021).
7. S. An, W. Zhao, A. Zhai, *et al.*, "Focusing through scattering media via 1D speckle signal feedback," Laser Photonics Rev. **19**, 2401101 (2024).
8. Y. Shi, W. Sheng, Y. Fu, *et al.*, "Overlapping speckle correlation algorithm for high-resolution imaging and tracking of objects in unknown scattering media," Nat. Commun. **14**, 7742 (2023).
9. S. Kang, Y. Kwon, H. Lee, *et al.*, "Tracing multiple scattering trajectories for deep optical imaging in scattering media," Nat. Commun. **14**, 6871 (2023).
10. I. Freund, M. Rosenbluh, and S. Feng, "Memory effects in propagation of optical waves through disordered media," Phys. Rev. Lett. **61**, 2328–2331 (1988).
11. H. Liu, Z. Liu, M. Chen, *et al.*, "Physical picture of the optical memory effect," Photonics Res. **7**, 1323–1330 (2019).
12. G. Osnabrugge, R. Horstmeyer, I. N. Papadopoulos, *et al.*, "Generalized optical memory effect," Optica **4**, 886–892 (2017).
13. M. Jang, H. Ko, J. H. Hong, *et al.*, "Deep tissue space-gated microscopy via acousto-optic interaction," Nat. Commun. **11**, 710 (2020).
14. S. Kang, S. Jeong, W. Choi, *et al.*, "Imaging deep within a scattering medium using collective accumulation of single-scattered waves," Nat. Photonics **9**, 253–258 (2015).
15. Y. Bian, F. Wang, Y. Wang, *et al.*, "Passive imaging through dense scattering media," Photonics Res. **12**, 134–140 (2024).
16. M. E. Zevallos L, S. K. Gayen, M. Alrubaiee, *et al.*, "Time-gated backscattered ballistic light imaging of objects in turbid water," Appl. Phys. Lett. **86**, 011115 (2005).
17. S. Li, S. A. R. Horsley, T. Tyc, *et al.*, "Memory effect assisted imaging through multimode optical fibres," Nat. Commun. **12**, 3751 (2021).
18. M. Nixon, O. Katz, E. Small, *et al.*, "Real-time wavefront shaping through scattering media by all-optical feedback," Nat. Photonics **7**, 919–924 (2013).
19. A. Boniface, M. Mounaix, B. Blochet, *et al.*, "Transmission-matrix-based point-spread-function engineering through a complex medium," Optica **4**, 54–59 (2017).
20. D. Feldkhun, O. Tzang, K. H. Wagner, *et al.*, "Focusing and scanning through scattering media in microseconds," Optica **6**, 72–75 (2019).
21. Z. Cheng and L. V. Wang, "Focusing light into scattering media with ultrasound-induced field perturbation," Light Sci. Appl. **10**, 159 (2021).
22. Z. Cheng, C. Li, A. Khadria, *et al.*, "High-gain and high-speed wavefront shaping through scattering media," Nat. Photonics **17**, 299–305 (2023).
23. Z. Cheng, J. Yang, and L. V. Wang, "Intelligently optimized digital optical phase conjugation with particle swarm optimization," Opt. Lett. **45**, 431–434 (2020).
24. Z. Zhang, X. Ma, and J. Zhong, "Single-pixel imaging by means of Fourier spectrum acquisition," Nat. Commun. **6**, 6225 (2015).
25. T. Zhang, Y. Xiao, and W. Chen, "Single-pixel microscopic imaging through complex scattering media," Appl. Phys. Lett. **126**, 031106 (2025).
26. Z. Wang, T. Zhang, Y. Xiao, *et al.*, "Common-path ghost imaging through complex media with dual polarization," Opt. Lett. **50**, 1152–1155 (2025).
27. W. Gong and S. Han, "Correlated imaging in scattering media," Opt. Lett. **36**, 394–396 (2011).

28. D. Zhang, W. Sheng, Y. Shi, *et al.*, “Imaging objects hidden inside the strongly scattering media based on bidirectional ghost imaging,” Opt. Lett. **49**, 13–16 (2024).
29. Y. Xiao, L. Zhou, and W. Chen, “High-resolution ghost imaging through complex scattering media via a temporal correction,” Opt. Lett. **47**, 3692–3695 (2022).
30. K. Song, Y. Bian, D. Wang, *et al.*, “Advances and challenges of single-pixel imaging based on deep learning,” Laser Photonics Rev. **19**, 2401397 (2024).
31. Y. Chen, Z. Sun, C. Li, *et al.*, “Computational ghost imaging in turbulent water based on self-supervised information extraction network,” Opt. Laser Technol. **167**, 109735 (2023).
32. F. Wang, C. Wang, C. Deng, *et al.*, “Single-pixel imaging using physics enhanced deep learning,” Photonics Res. **10**, 104–110 (2022).
33. B. Liu, F. Wang, C. Chen, *et al.*, “Self-evolving ghost imaging,” Optica **8**, 1340–1349 (2021).
34. L. Pan, Y. Shen, J. Qi, *et al.*, “Single photon single pixel imaging into thick scattering medium,” Opt. Express **31**, 13943–13958 (2023).
35. A. M. Paniagua-Diaz, I. Starshynov, N. Fayard, *et al.*, “Blind ghost imaging,” Optica **6**, 460–464 (2019).
36. F. Li, M. Zhao, Z. Tian, *et al.*, “Compressive ghost imaging through scattering media with deep learning,” Opt. Express **28**, 17395–17408 (2020).
37. X. Zhao, X. Nie, Z. Yi, *et al.*, “Imaging through scattering media via spatial–temporal encoded pattern illumination,” Photonics Res. **10**, 1689–1694 (2022).
38. B. Luo, P. Yin, L. Yin, *et al.*, “Orthonormalization method in ghost imaging,” Opt. Express **26**, 23093–23106 (2018).
39. R. Joshi, G. Krishnan, T. O’Connor, *et al.*, “Signal detection in turbid water using temporally encoded polarimetric integral imaging,” Opt. Express **28**, 36033–36045 (2020).
40. B. Redding, M. A. Choma, and H. Cao, “Speckle-free laser imaging using random laser illumination,” Nat. Photonics **6**, 355–359 (2012).
41. F. Ferri, D. Magatti, L. A. Lugiato, *et al.*, “Differential ghost imaging,” Phys. Rev. Lett. **104**, 253603 (2010).
42. B. Sun, S. S. Welsh, M. P. Edgar, *et al.*, “Normalized ghost imaging,” Opt. Express **20**, 16892–16901 (2012).
43. J. Schoukens and J. Renneboog, “Modeling the noise influence on the Fourier coefficients after a discrete Fourier transform,” IEEE Trans. Instrum. Meas. **IM-35**, 278–286 (1986).